EXPERIMENTAL INVESTIGATION OF FRICTION DAMPING IN BLADE ROOT JOINTS

Original
EXPERIMENTAL INVESTIGATION OF FRICTION DAMPING IN BLADE ROOT JOINTS / Botto, D., Iannotti, V., Cuccovillo, F.. - ELETTRONICO. - 8-B:(2022). (ASME Turbo Expo 2022: Turbomachinery Technical Conference and Exposition, GT 2022 Rotterdam (Netherlands) 2022) [10.1115/GT2022-81663].

Publisher:
American Society of Mechanical Engineers (ASME)

Published
DOI:10.1115/GT2022-81663

Proceedings of the ASME Turbo Expo 2022
Turbomachinery Technical Conference and Exposition
GT2022
June 13–17, 2022, Rotterdam, The Netherlands

GT2022-81663

EXPERIMENTAL INVESTIGATION OF FRICTION DAMPING IN BLADE ROOT JOINTS

Daniele Botto[*]
Department of Mechanical and
Aerospace Engineering
Politecnico di Torino
10129 Torino, Italy
daniele.botto@polito.it

Veronica Iannotti
Department of Mechanical and
Aerospace Engineering
Politecnico di Torino
10129 Torino, Italy
veronica.iannotti@polito.it

Federica Cuccovillo
Department of Mechanical and
Aerospace Engineering
Politecnico di Torino
10129 Torino, Italy
federica.cuccovillo@polito.it

ABSTRACT

The design of disk assemblies requires the capability to predict their dynamic behavior. To achieve this objective, knowledge of friction damping on the contact between blade and disk is of paramount importance. This paper proposes an experimental technique to measure the loss factor and the dynamics, in terms of natural frequencies, of blade-disk attachment. The free decay is used to infer the dynamic parameters from dummy blades. The identification method is based on the Hilbert transform that allows extracting the dynamic parameters from non-linear system. This paper shows the test rig utilized in the experimental analysis and details the excitation system used to displace the dummy blade. This system must be a real or a "virtual" non-contact system to avoid injecting external damping into the blade under test. Tests were performed on both a dovetail and a fir-tree type attachments. On the dovetail, tests were performed both with dry contact surfaces and with contact surfaces covered by a film of lubricant to achieve a low coefficient of friction. This low coefficient of friction better simulates dry surfaces at high temperatures, as friction coefficients decrease with temperatures. This paper presents the results obtained on the first and second bending mode. The experimental results show the loss factor and the natural frequency for different axial loads. The measured loss factor depends on the amplitude of vibrations. As predicted with theoretical analyses the loss factor shows a maximum then approaching zero for large amplitude of vibrations. As a rule, it decreases with increasing centrifugal loads.

INTRODUCTION

Background

Fatigue failure of blades caused by vibrations is a major concern for aircraft engine designers [1]. To keep the vibration level below a critical value the dynamic behavior of the blade, in terms of modal damping, must be well characterized. In addition to damping due to inherent material properties, referred to as internal or structural damping, not negligible contributions come from friction damping resulting from contact interfaces at shrouds, blade attachments or additional devices such as under-platform dampers [2]. Friction damping is a phenomenon in which mechanical work is dissipated and damping occurs. The mechanical work is done by the tangential force generated by the friction and the relative motion between the two contact surfaces. As a side effect, the contact forces and their relative displacement could induce fretting fatigue [3] or fretting wear [4]. The friction force is modeled, in its simplest form, with a piecewise function that triggers a non-linear behavior of the blade response [5].

Several works can be found in the literature dealing with experimental measurements of blade root damping properties. One of the first study on friction damping at blade root was proposed in [6] in which the authors presented a general theory of slip damping and found an expression for the energy loss per cycle of oscillation. Experiments were performed on an uniform-pressure joint an the oscillating motion was obtained with a vibration exciter made with an eccentric. They concluded that slip damping at the root provides a highly beneficial reduction of vibrations, especially in condition where aerodynamic damping is inade-

---

[*] Address all correspondence to this author.

quate. In [7] a dovetail root was used to clarify the effect of gross slip on the dynamic response under harmonic oscillations. The authors performed an experimental investigation where the normal load at the dovetail was provided by thin wires and the blade was excited by a shaker. Tests were performed in air and water and transfer functions were measured with miniature accelerometers. The modal damping was measured with the half power method. Experimental results were compared with an analytical model solved with the harmonic balance method. One section in report [8] presents the results of a numerical simulation and tests carried out on a fan blade with a dovetail root. The centrifugal load is applied by a loading screw pushing the root of a blade against the slot and measuring the load with strain gauges on the stem. A similar system was used also in [9] and [10] with the pushing load measured with a load cell. A sinusoidal excitation was applied through a shaker at the blade root and the blade response was monitored via strain gages mounted at high stress points. The response was measured after abrupt cut off of input shaker signals. This idea also drives the present work. The level of damping was estimated from the slope of the resulting decay curve. The same author [11] presented a in-depth study of blade vibration problems and their influence on the structural integrity of power plants. An interesting idea was presented in [12] where the centrifugal load was applied providing an initial mismatch between the contact surfaces at the blade root that is removed by thermal expansion. The centrifugal load is obtained after cooling the assembly. Damping properties were measured with free vibration in the time domain. The damping ratio was presented as a function of the vibratory relative amplitude for different axial loads. The work presented in [13] describes a series of experiment to examine the damping properties of steam turbine blade roots. Tests were conducted in a non-rotating rig with pairs of real blades welded together at the tip. The tensile preload was developed using thermal shrinkage. The logarithmic decrement was measured through vibration decay tests and was found approximately linearly-related to the vibration amplitude at the blade tip. In [14] a dummy blade with attachments at both ends is assembled in slots supported by two cross beams. An hydraulic cylinder applied the centrifugal load by moving one of the cross beam while vibrations were induced by using an electromagnetic exciter. As the magnetic force is proportional to the square of the current in the coil the current frequency must be half the frequency of the desired exciting force. The work presented in [15] analyzed the impact of friction in blade attachments on the forced response of blades. A rotating disk was tested in vacuum and swept sine excitation was provided by piezoelectric actuators. The frequency response was measured by strain gauges and the amount of damping was computed with the half power bandwidth method. An efficient multi harmonic balance method was proposed to compute the forced response.

Objective

The main goal of this work is a better understanding of the phenomena related to the blade-root damping. To pursue this goal an experimental campaign was launched to measure the free decay of a dummy blade with dovetails at both end under different load conditions.

The main innovative feature of this work is the virtual non-contact excitation system that was specifically developed for this test campaign. This system utilizes a shaker in which the drive rod is not integral with the assembly to be excited. The drive rod is abruptly removed from the assembly before recording the free decay. In this way the no external noise or damping are injected into the system under investigation, signals are cleaner, and better results can be achieved. Data were post-processed with the method proposed in [16] to derive the natural frequency and the loss factor. Data were collected by using the same test rig described in [14].

FREQUENCY AND DAMPING IDENTIFICATION

The dependence of the natural frequency and damping on the amplitude of vibration, typical of nonlinear behavior, can be obtained from a free decay test with the method proposed in [16].This method works in the time domain and is based on the analytic signal *Y(t)* corresponding to the real signal *y(t)*

$$Y(t) = y(t) + i\tilde{y}(t) = A(t) \cdot e^{i\varphi(t)} \tag{1}$$

where $\tilde{y}(t)$

$$\tilde{y}(t) = H[y(t)] = \frac{1}{\pi t} * y(t) = \frac{1}{\pi}\int_{-\infty}^{+\infty} \frac{y(t)}{t-\tau} d\tau \tag{2}$$

is the Hilbert transform of *y(t)*. The terms *A(t)* and *φ(t)* in Eqn. (1) are the instantaneous amplitude and instantaneous phase of the analytic signal *Y(t)* respectively.

Dry friction is the dominant source of damping in blade attachments. Friction forces undergoing oscillating motion generate hysteresis loops as sketched in Fig. 4. Analysis of energy dissipation in hysteresis loops lead to the conclusion that dry friction can be classified as a frequency-dependent damping. This kind of damping is denoted to as hysteretic damping and in dynamic model it is equivalent to an imaginary stiffness. The dynamic equation of motion with hysteretic damping can be written as

$$m\ddot{y} + (k(A) + ih(A))\,y = 0 \tag{3}$$

In Eqn. (3) the stiffness *k(A)* and the hysteretic damping *h(A)* are unknown functions and, for non linear systems, depend on the amplitude of vibration A. Applying the Hilbert transform to Eqn. (3) the dynamic equation of motion becomes

$$m\ddot{\tilde{y}} + (k(A) + ih(A))\,\tilde{y} = 0 \tag{4}$$

Multiplying each term of Eqn. (4) by the imaginary unit i and adding it to the corresponding term of Eqn. (3) we obtain the analytic form of the equation of motion

$$m\ddot{Y} + (k(A) + ih(A))\,Y = 0 \tag{5}$$

Equation (5) can be rewritten

$$\ddot{Y} + \omega_n^2(A)\,(1 + i\eta(A))\,Y = 0 \tag{6}$$

with

$$\omega_n^2(A) = \frac{k(A)}{m} \tag{7a}$$

$$\eta(A) = \frac{h(A)}{k(A)} \tag{7b}$$

the instantaneous natural frequency and the loss factor respectively, also referred to as modal parameters. The first and second derivative of the analytic signal in Eqn. (1) are

$$\dot{Y} = \dot{y} + i\dot{\tilde{y}} = (y + i\tilde{y})\left[\frac{\dot{A}}{A} + i\omega\right] \tag{8a}$$

$$\ddot{Y} = \ddot{y} + i\ddot{\tilde{y}} = (y + i\tilde{y})\left[\frac{\ddot{A}}{A} - \omega^2 + i2\omega\frac{\dot{A}}{A} + i\dot{\omega}\right] \tag{8b}$$

where $\omega = \dot{\varphi}(t)$ is the instantaneous frequency of the signal. By substituting Eqn. (8b) into Eqn. (5) the dynamic equation of motion becomes

$$\left[\frac{\ddot{A}}{A} - \omega^2 + \omega_n^2 + i\left(2\omega\frac{\dot{A}}{A} + \dot{\omega} + \omega_n^2\eta\right)\right] Y = 0 \tag{9}$$

By solving two equation for the real and imaginary parts of Eqn. (9) we obtain the expression for the two unknown parameters

$$\omega_n^2(A) = \omega^2 - \frac{\ddot{A}}{A} \tag{10a}$$

$$\eta(A) = -\frac{1}{\omega_n^2}\left(2\omega\frac{\dot{A}}{A} + \dot{\omega}\right) \tag{10b}$$

The terms on the right-hand side of Eqn. (10) can be evaluated using the measured signal *y(t)* and its Hilbert trasform $\tilde{y}(t)$. The first derivative Eqn. (8a) gives the free vibration frequency ω and the ratio $\dot{A}/A$

$$\omega(t) = \frac{1}{A^2}\left(y\dot{\tilde{y}} - \dot{y}\tilde{y}\right) \tag{11a}$$

$$\frac{\dot{A}}{A}(t) = \frac{1}{A^2}\left(y\dot{y} + \tilde{y}\dot{\tilde{y}}\right) \tag{11b}$$

while the second derivative in Eqn. (8b) gives the variation of free vibration frequency $\dot{\omega}$ and the ratio $\ddot{A}/A$

$$\dot{\omega}(t) = \frac{y\ddot{\tilde{y}} - \tilde{y}\ddot{y}}{A^2} - 2\omega\frac{\dot{A}}{A} \tag{12a}$$

$$\frac{\ddot{A}}{A}(t) = \frac{y\ddot{y} + \tilde{y}\ddot{\tilde{y}}}{A^2} + \omega^2 \tag{12b}$$

The right-hand side in Eqn. (11) and (12) depends on the Amplitude *A(t)* that can be evaluated as

$$A(t) = \sqrt{y^2 + \tilde{y}^2} \tag{13}$$

EXPERIMENTAL MEASUREMENTS

Test Rig

Figure 1 depicts the working scheme of the test rig used in the present work. The complexity of generating the centrifugal load through a rotating rig led to the development of a static loading technique. The unfeasibility of statically pulling a real blade without introducing additional damping is the reason of the symmetry of the rig, in which a dovetail type attachment is machined at both ends of a beam with constant rectangular cross-section to create the dummy blade. The equivalence of loads and joint kinematics makes the results obtained on this rig comparable with those on a real disk. More detailed considerations on the design principle of the rig can be found in [14].

The attachments are fitted into the slots machined in two supports. These supports are integral with two crossbars: one crossbar is fixed while the other is free to move if loaded with an axial force. The axial force F_{ax} is exerted through a hydraulic cylinder operated by a manual pump. The axial force is measured with two independent systems. A pressure gauge is connected to the hydraulic cylinder and its value is read directly by the operator. A full-bridge strain gauge is attached with adhesive to the dummy blade and it is read by a signal conditioning card and stored by the Data AcQuisition (DAQ) system. The dynamic excitation system is composed by an electrodynamic shaker and its power amplifier. This amplifier is fed with a signal produced by a wave form generator. The drive rod of the shaker is not

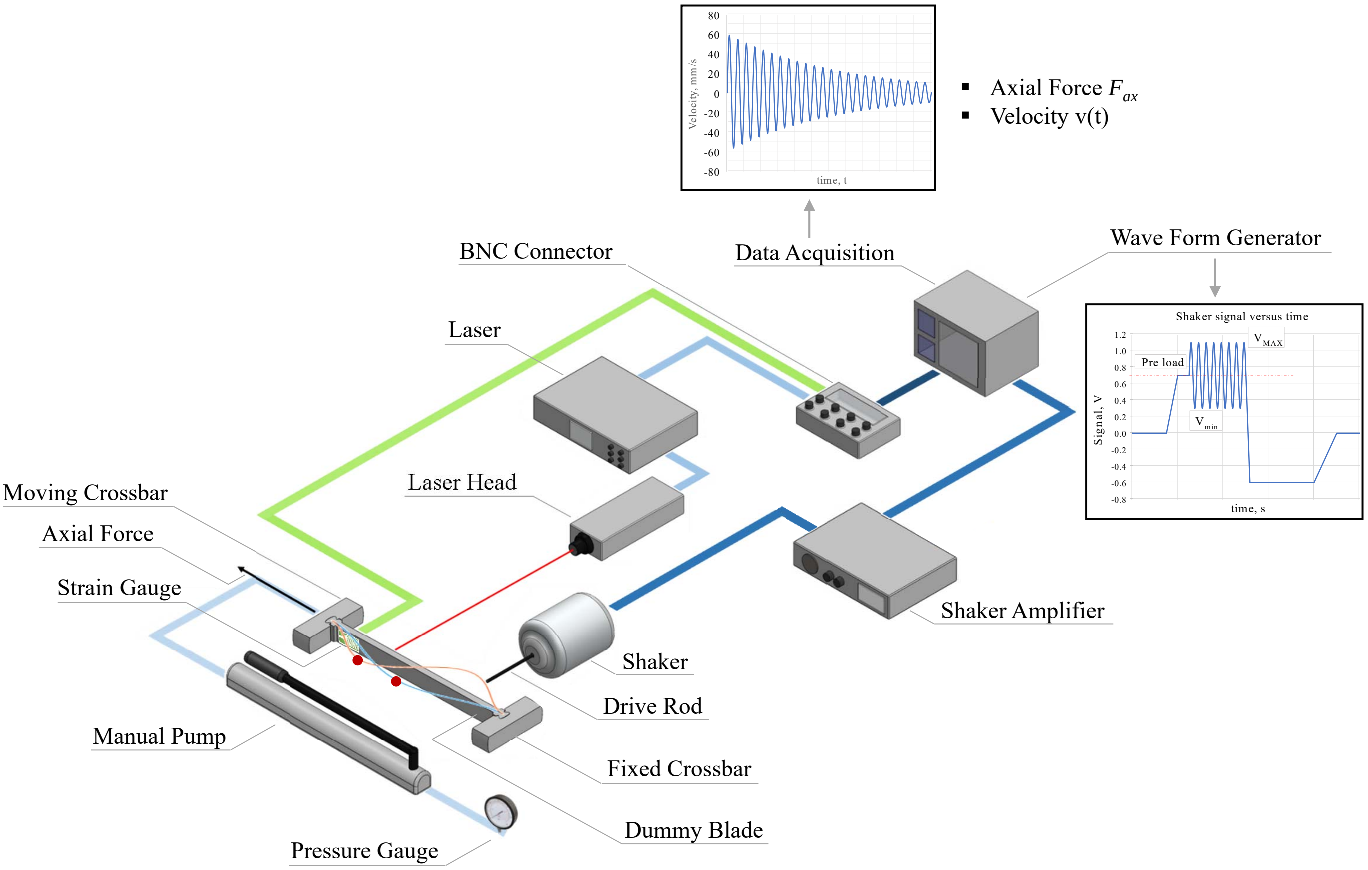

FIGURE 1. SCHEME OF THE TEST RIG UTILIZED IN THE EXPERIMENTAL CAMPAIGN.

fixed to the dummy blade but it can be brought into contact or released by displacing the moving coil of the shaker. Beforehand, the drive rod is displaced by a wave form consisting of a ramp followed by a positive constant value. A proper choice of the initial gap between the drive rod and the dummy blade together with the value of the constant signal allows the drive rod to preload the dummy blade. The preload is followed by a sinusoidal wave whose frequency is chosen as close as possible to the resonance of the modal shape under investigation. If the preload has been properly defined the drive rod remains in contact with the dummy blade during the sinusoidal excitation period. At the end of the excitation period the drive rod is suddenly detached, with a negative wave form signal, from the dummy blade that from this point on is free to oscillate so that no additional damping injected by the shaker. This method will be referred to as the Detached Drive Rod Method (DDRM). The excitation system used in this work differs from the one used in [14] in which the dummy blade was loaded with non-contact exciter based on electromagnets. The main objective of both systems is the same: to uncouple the dummy blade from the exciter so that no additional damping is injected during the free decay. With the non-contact exciter this objective is achieved by stopping the current in the coil whereas with the DDRM the drive rod is physically detached from the contact point. The main advantage of using the DDRM is that the excitation force is applied at a specific point and can be measured with a load cell if the forced-response is needed. The non-contact exciter needs a complex calibration process to measure the transfer function between the force measured on the electromagnet and the true force applied to the dummy blade, as well explained in [17].

A Laser Doppler Vibrometer together with its controller measures the velocity of one reference point at time on the dummy blade. This vibrometer features digital signal processing that enables high-precision and high-resolution vibration acquisition. The resolution of the velocity can be translated into the corresponding amplitude resolution, and, at the frequency of interest, the obtained value is approximately less than 3 pm. The DAQ system collects and records point velocity and strain gauge signals. This system is based on a 8 channel analog inputs card (simultaneous sampling at 1.25 MS/s/ch, 16-bit resolution). The accuracy of the card, in the voltage range ±10V, is 3 mV thus giving an accuracy ±0.08 μm on the measured amplitude in the frequency range of interest. The wave form is created with a in-house code with a sampling rate of 10 kHz and stored on file. This file is then read by the wave form generator that provides the output voltage signal.

The main differences between real blades and the dummy blade are listed below.

- A real blade has only one joint and its modal shapes are approximately like those of a cantilever beam, while the simplified system under test is like a fixed-fixed beam. In addition, the geometries of the cross sections of the real and dummy blades are different.
- The centrifugal force acting on a section of a real blade decreases with the distance from the joint. In contrast the tensile load acting on the studied dynamic system is constant along its main axis.

Because of these differences, the test rig can provide qualitative rather than quantitative results on the damping due to the blade-disk joint and the dependence of damping on vibration amplitude and centrifugal force. But, since the energy dissipated at the joint depends on the forces acting on a blade cross-section near the joint, the dummy blade studied here dissipates the same energy as a blade that has the same resultant forces acting on the joint, even though the mode shape is different. In addition, the test-rig allows the dissipated energy and damping to be calculated. These values can be compared with those obtained from numerical models of the system, so modeling techniques for dynamic systems with blade-disk joints can be verified.

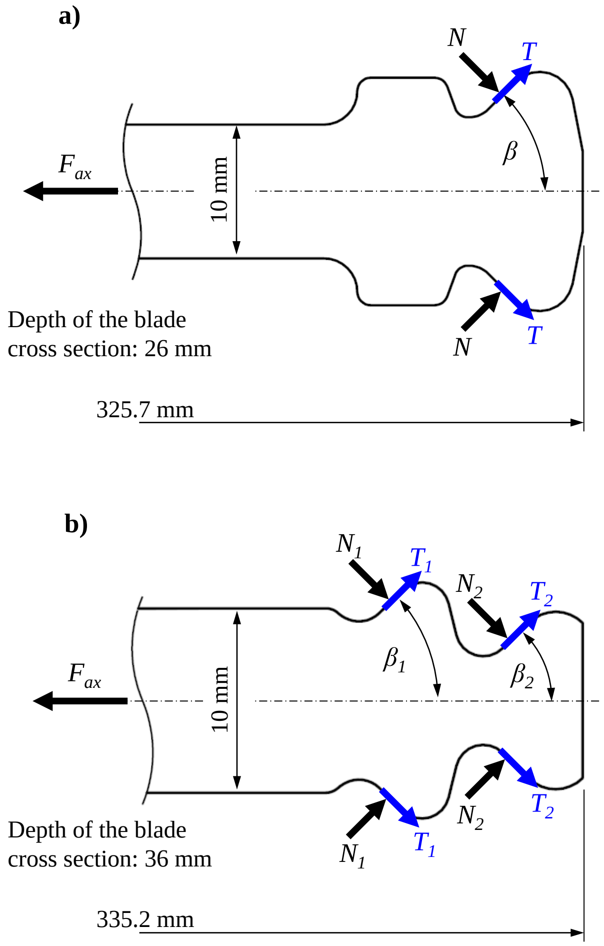

FIGURE 2. FORCES ACTING ON AND MAIN DIMENSIONS OF DOVETAIL AND FIR-TREE ATTACHMENTS.

Testing procedure

Experiments were focused on the free decay of oscillations of the first and second bending mode of the dummy blade. Velocity was measured at the antinode of the modal shape under investigation. For both modes a set of measurements at different axial loads F_{ax} was carried out. The testing procedure for each measurement is described in the following.

1. The dummy blade is pulled with the axial load F_{ax}, which is evaluated with the pressure gauge and strain gauges through the formulae

   $$F_{ax} = A_{cyl}\, p \tag{14a}$$

   $$F_{ax} = A_{beam}\, \sigma = A_{beam}\, E_{st}\, \varepsilon \tag{14b}$$

   where A_{cyl} = 1790 mm ^{2} is the effective area of the hydraulic cylinder, p is the measured pressure, A_{beam} = 26 x 10 mm^2 is the rectangular cross-section of the dummy blade, E_{st} = 200.3 GPa the Young Modulus of the blade material (steel) and ε the measured strain. Two dummy blades were used, one with a dovetail and the other with a fir-tree attachment. The geometry of the attachments and their main dimensions are depicted in Fig. 2. The uncertainty on the measured axial load F_{ax} due to pressure gauge accuracy is ± 1%.

   As reported in [14], on real engines in cruise condition a typical centrifugal load on blades is about 50 kN. The minimum load, during the flight descent phase when the engine runs at idle speed, is about 2.5 kN. In the present work measurements were performed with tensile loads up to 25 kN, a value that is representative of the real operating condition.
2. A preliminary hammer test is performed on the loaded dummy blade to obtain a first estimate of the natural frequencies of the first two bending modes.
3. The loaded dummy blade is excited by using the DDRM with an oscillating force whose frequency was estimated as in point 2. The free vibrations is obtained once the drive rod

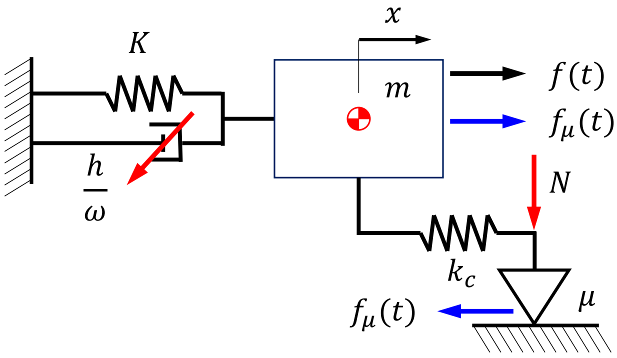

FIGURE 3. SINGLE DEGREE OF FREEDOM SYSTEM WITH DRY FRICTION CONTACT.

is detached from the excitation point.

4. The useful portion of the velocity *v(t)* is limited to the interval of free decay. This portion of the signal is filtered with a band-pass FIR filter: a minimum-order linear-phase filter with pass-band frequency range centered on the frequency of the examined mode is designed.
5. The filtered signal is processed with the method described in [16]. In the present work, the measured signal is the velocity $v(t) = \dot{y}(t)$. Thus, displacement $y(t)$ and acceleration $\ddot{y}(t)$ are computed by numerical integration and differentiation of *v(t)* respectively. The results, in term of frequency and loss factor, are smoothed with a moving average filter to avoid artifacts at high amplitudes.

SINGLE DEGREE OF FREEDOM MODEL

To better understand the experimental results a simple simulation on a single degree of freedom (dof) has been performed. The single dof system is depicted in Fig. 3. The mass m is constrained by the stiffness K and the term h/ω variable with frequency ω, accounts for damping sources other than friction, such as material hysteresis. The mass is connected to a contact point through a Jenkins element, whose contact stiffness is k_c and friction coefficient μ, loaded with a normal load N. The dynamic equation of equilibrium of the system is

$$m\ddot{x} + \frac{h}{\omega}\dot{x} + Kx + f_\mu(t) = f_{ext}(t) \tag{15}$$

where $f_\mu(t)$ is the piecewise defined friction force

$$f_\mu = \begin{cases} k_c \cdot x & \text{if} \quad |k_c \cdot x| \le \mu N \\ \mu N & \text{if} \quad |k_c \cdot x| > \mu N \end{cases} \tag{16}$$

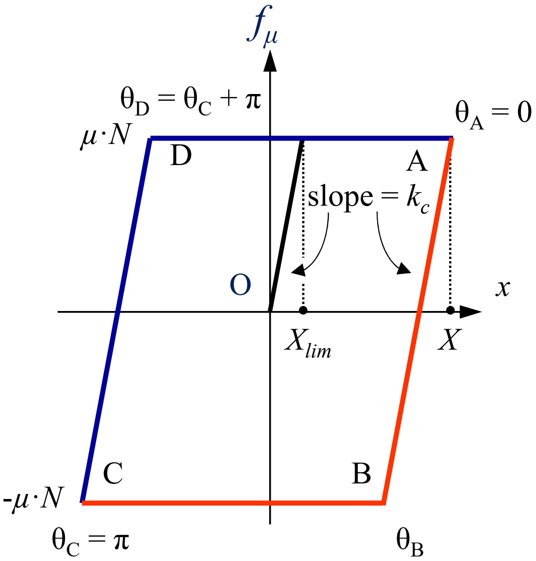

FIGURE 4. HYSTERESIS LOOP ASSOCIATED TO A SINGLE JENKINS ELEMENT WITH COULOMB FRICTION.

The friction force as defined in Eqn. (16) produces the hysteresis loop depicted in Fig. 4 under the action of an oscillating external force. The steady-state solution of Eqn. (15) can be found by using the Harmonic Balance Method (HBM) as proposed in [18]. A trial solution $x = X\cos(\omega t)$ is substituted into Eqn. (15) with the phase transferred onto the external force $f = F\cos(\omega t - \phi)$ to allow the magnitude X to be taken as real and without losing generality. According to the treatment done in [19] the angle θ_B (associated to point B in the hysteresis loop in Fig. 4) is

$$\theta_B = \omega t_B = \arccos\left(1 - \frac{2\mu N}{k_c X}\right) \tag{17}$$

The friction force can be approximated by a one-term Fouries transform whose cos and sin components can be found as

$$f_{\mu 1c} = \frac{2}{\pi}\int_0^\pi f_\mu \cos\theta \, d\theta \tag{18a}$$

$$f_{\mu 1s} = \frac{2}{\pi}\int_0^\pi f_\mu \sin\theta \, d\theta \tag{18b}$$

Substituting Eqn. (16) into Eqn. (18) gives the values of the Fourier components

$$f_{\mu 1c} = \frac{k_c X}{\pi}\left(\omega t_B - \frac{1}{2}\sin(2\omega t_B)\right) \tag{19a}$$

$$f_{\mu 1s} = \frac{-4\mu N}{\pi}\left(1 - \frac{\mu N}{k_c X}\right) \tag{19b}$$

By substituting the first order approximation of the friction force as in Eqn. (19) and the trail solution Eqn. (15) gives

$$-\omega^2 m\cos(\omega t)-\left(h-\frac{f_{\mu 1s}}{X}\right)\sin(\omega t)+\left(K+\frac{f_{\mu 1c}}{X}\right)\cos(\omega t)= \\ =\frac{F}{X}\cos(\omega t-\phi) \quad (20)$$

From Eqn. (20) it is clear that the effect of the friction force is to add stiffness and hysteretic damping to the system. The total stiffness and damping are

$$K_{tot}=K+\frac{k_c}{\pi}\left(\omega t_B-\frac{1}{2}\sin(2\omega t_B)\right)=K+k_{eq} \quad (21a)$$

$$h_{tot}=h+\frac{4\mu N}{\pi X}\left(1-\frac{\mu N}{k_c X}\right)=h+h_{eq} \quad (21b)$$

Equations (21) can be normalized with the stiffness K and rewritten as

$$\frac{K_{tot}}{K}=1+\frac{1}{\pi}\frac{k_c}{K}\left(\omega t_B-\frac{1}{2}\sin(2\omega t_B)\right) \quad (22a)$$

$$\eta=\frac{h_{tot}}{K}=\eta_0+\frac{4}{\pi}\frac{X_{lim}}{X}\frac{k_c}{K}\left(1-\frac{X_{lim}}{X}\right) \quad (22b)$$

where η_0 accounts for damping sources other than friction such as hysteresis, while

$$X_{lim}=\frac{\mu N}{k_c} \quad (23)$$

is the displacement at the onset of sliding. The normalized stiffness and the loss factor are function of two dimensionless variables, namely the ratios X_{lim}/X and k_c/K, as also the angle ωt_B depends only on the ratio X_{lim}/X, see Eqn. (17).

Figures 5 and 6 show the loss factor, according to Eqn. (22b), and the ratio K_{tot}/K, Eqn. (22a), respectively. Calculation were performed with different contact stiffness k_c and limit displacement X_{lim} applied to the same single dof system, that means same η_0 and K. The arrow in the figures indicates decreasing contact stiffness and increasing limit displacement.

For displacements less than X_{lim} the system is in stick conditions then the loss factor coincide with η_0 whereas the total stiffness is given by $K + k_c$. When the displacements exceed X_{lim} the loss factor increases to a maximum and then asymptotically decreases to η_0. The limit displacement X_{lim} merely translates the position of the loss factor peak but it has no effect on its maximum value. This result is consistent with the results presented in [6]. The value of the loss factor peak is driven by the stiffness ratio k_c/K: the higher the ratio the higher the peak. The total stiffness K_{tot} monotonically decreases with the displacement X approaching K for very large displacement.

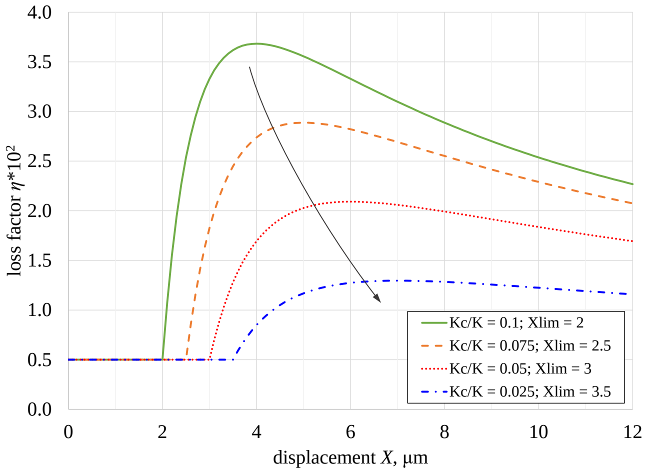

FIGURE 5. THEORETICAL LOSS FACTOR η AS A FUNCTION OF THE DISPLACEMENT AMPLITUDE X IN A SINGLE DEGREE OF FREEDOM SYSTEM. CURVES DIFFER IN THE STIFFNESS RATIO k_c/K AND LIMIT DISPLACEMENT X_{lim}.

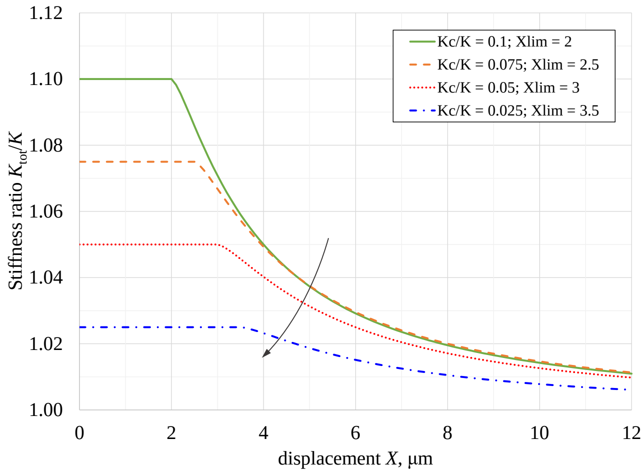

FIGURE 6. THEORETICAL STIFFNESS RATIO K_{tot}/K AS A FUNCTION OF THE DISPLACEMENT AMPLITUDE X IN A SINGLE DEGREE OF FREEDOM SYSTEM. CURVES DIFFER IN THE STIFFNESS RATIO k_c/K AND LIMIT DISPLACEMENT X_{lim}.

RESULTS AND DISCUSSION

Results are given in term of loss factors and natural frequency at varying axial loads. Figure 7 shows the loss factor for

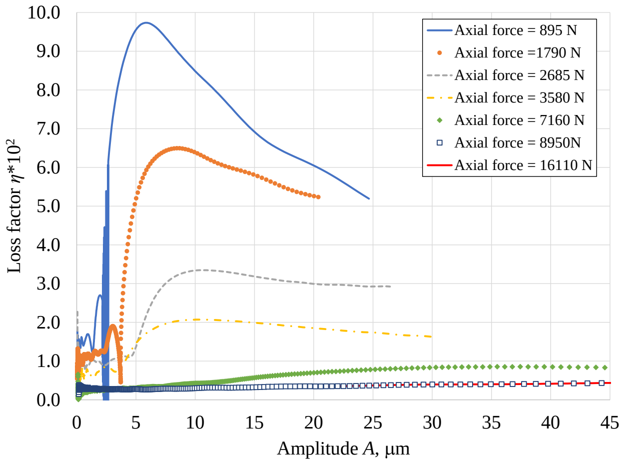

FIGURE 7. MEASURED LOSS FACTOR η AS A FUNCTION OF THE DISPLACEMENT OF THE ANTINODE FOR THE FIRST MODE. CURVES DIFFER IN AXIAL FORCE.

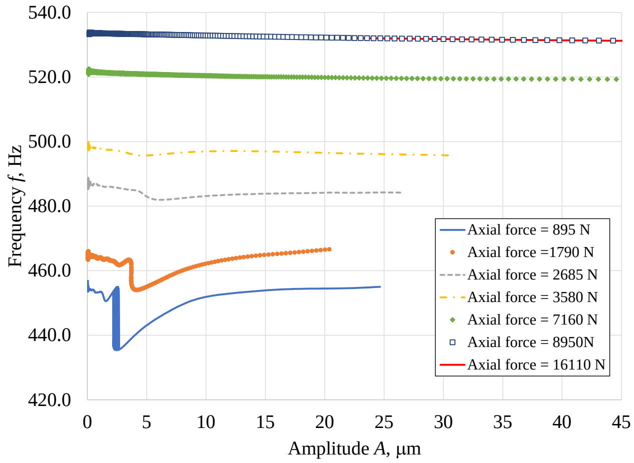

FIGURE 8. MEASURED NATURAL FREQUENCY AS A FUNCTION OF THE DISPLACEMENT OF THE ANTINODE FOR THE FIRST MODE. CURVES DIFFER IN AXIAL FORCE.

the first bending mode. Curves clearly show the stick condition for low amplitude in which the loss factor remains constant. Exceeded the limit X_{lim} the loss factor increases with amplitude A up to a peak and then it decreases. The peak value decreases while the peak position moves toward higher amplitude as axial loads increase. This behavior is consistent with what predicted by the single degree of freedom model. The stiffness of the dummy blade and the contact stiffness increase with axial loads. It will be shown later that the contact stiffness increases less than the stiffness of the dummy blade so that the ratio k_c/K diminish with axial loads. Moreover, increasing the axial load means increasing the limit displacement X_{lim} and this translates in peaks moving towards greater amplitudes. The loss factor induced by the dovetail shows an appreciable increment with respect to the loss factor of the system with no friction element (η_0, deducible by the value at very low amplitude) up to axial loads approximately 7 kN. Tests were performed with axial loads up to 27 kN but for loads greater than approximately 9 kN the loss factor remains constant and loss factors at 8950 N and 16110 N show negligible differences. As reported in [14], on real engines under cruise condition a typical centrifugal load on the blade is about 50 kN. To induce slip conditions, and then a non negligible damping, for axial force greater than 9 kN most likely the excitation force would have to be greater than the force that can be applied with the current excitation system.

Figure 8 shows the natural frequency of the first mode of the dummy blade. The stick condition is represented by a constant frequency at low amplitude. This phenomenon is more evident at low axial loads while at high loads the blade root is in stick condition even at high amplitudes and the stick-slip transition is less distinguishable. A marked drop in frequency is observed during the transition between the stick and the slip condition. This drop becomes less evident with increasing axial loads and it is not predicted by the single dof model.

Figure 9 shows the natural frequencies for low displacement amplitude A of the first mode as a function of the axial force. The measured frequencies are compared with the result of a calculation performed with a FE model of the dummy blade and its supports. In the FE model contact the nodes are bonded, which is a stiffer condition than the real contact. Therefore, the calculated natural frequencies are higher than the experimental results. In addition, the calculated and experimental natural frequencies increase linearly with axial force due to the stiffening effect of axial loading. Experimental results empathize that where the slip regime is predominant, below 10000 N, the natural frequency increases non linearly and its slope decreases with the axial force. If the stick regime is predominant the natural frequency increases linearly with a slope very close to the slope of the blade with bonded joints. This behavior means that the contact stiffness k_c increases less than the stiffness of the dummy blade K and then the ratio k_c/K decreases with the axial force. This evidence supports the statement done in the previous paragraph to justify the peak decrease of the loss factor with increasing axial forces.

Additional test with a reduced friction coefficient were carried out to better investigate the theoretical behavior emphasized by the single dof model. The reduced friction coefficient was obtained by covering the contact surfaces with a thin film of 5W-40 lubricant. Tests were performed in the same load condition as in the dry friction surfaces. Figure 10 compares the results of the test with and without oil in terms of loss factor. It is evident from the comparison that the sliding condition occurs for smaller amplitude A as predicted by the simplified model where X_{lim} is

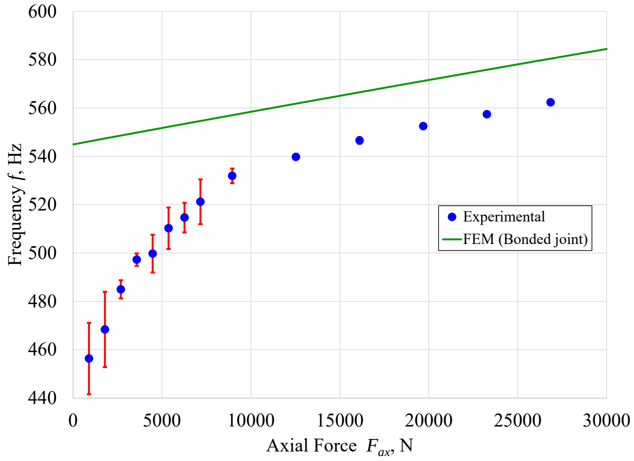

FIGURE 9. NATURAL FREQUENCY FOR LOW DISPLACEMENT AMPLITUDE *A* OF THE FIRST MODE. FREQUENCIES ARE PLOTTED AS A FUNCTION OF THE AXIAL FORCE AND WITH 2.58σ BARS.

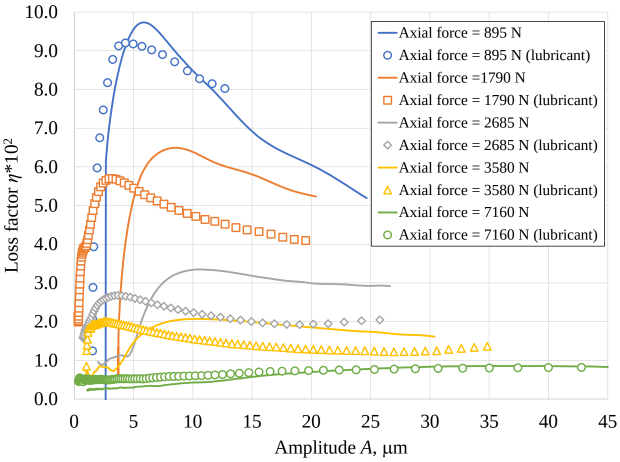

FIGURE 10. COMPARISON OF THE LOSS FACTOR MEASURED ON THE FIRST MODE OF THE DOVETAIL WITH AND WITHOUT LUBRICANT.

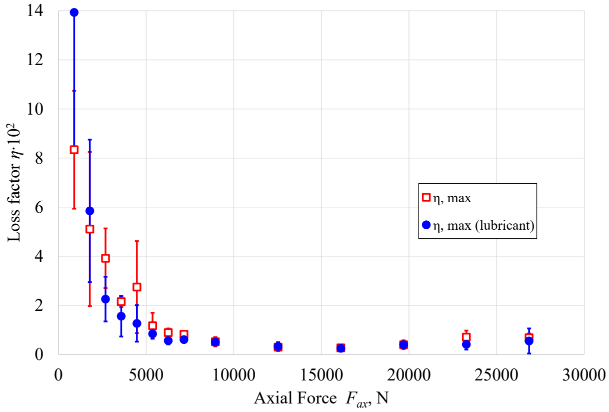

FIGURE 11. MAXIMUM LOSS FACTOR MEASURED ON THE FIRST MODE OF THE DOVETAIL WITH AND WITHOUT LUBRICANT. 2.58σ BARS ARE ALSO PLOTTED.

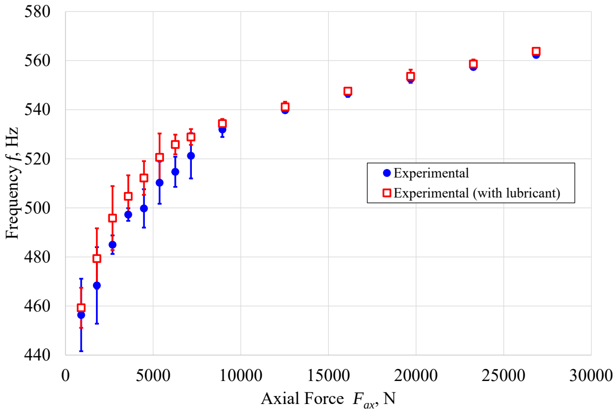

FIGURE 12. COMPARISON OF THE NATURAL FREQUENCIES MEASURED ON THE FIRST MODE WITH AND WITHOUT LUBRICANT AT THE DOVETAIL. 2.58σ BARS ARE ALSO PLOTTED.

proportional to the friction coefficient, see Eqn. (23). According to the simplified model the loss factor with lubricated surfaces reaches its peak for smaller amplitude than in the dry friction condition. The maximum loss factor does not appear to be affected by the coefficient of friction, and the lubricated surfaces show peaks comparable to the dry surfaces. Figure 11 shows the maximum loss factor as a function of axial loads. The maximum loss factor shows a similar trend and similar values for dry and lubricated surfaces. High scatter in the data is common since the results depend on the friction coefficient which is a highly random variable.

A second comparison was performed on the natural frequencies measured at small amplitude, a condition close to stick regime. Figure 12 shows the comparison. Unexpectedly, the natural frequencies with lubricated contact surfaces show higher natural frequencies especially at low axial forces. The difference in 2.5% in the worst case, corresponding to 11 Hz. At high axial force the natural frequencies show a negligible difference. This phenomenon can be explained by the lubricant meatus increasing the contact surface and consequently the contact stiffness. At high load the lubricant is ejected from the contact surface and its

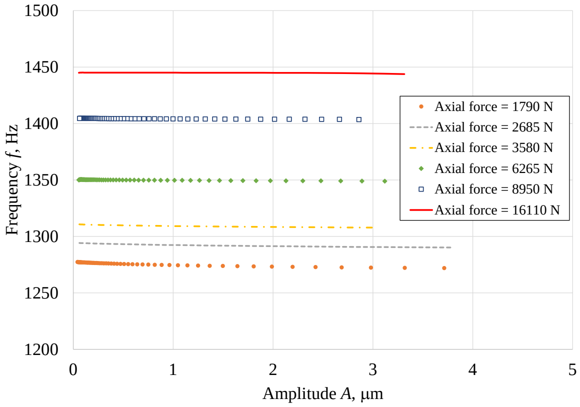

FIGURE 13. NATURAL FREQUENCY MEASURED AS A FUNCTION OF ANTINODE DISPLACEMENT FOR THE SECOND MODE ON THE DOVETAIL.

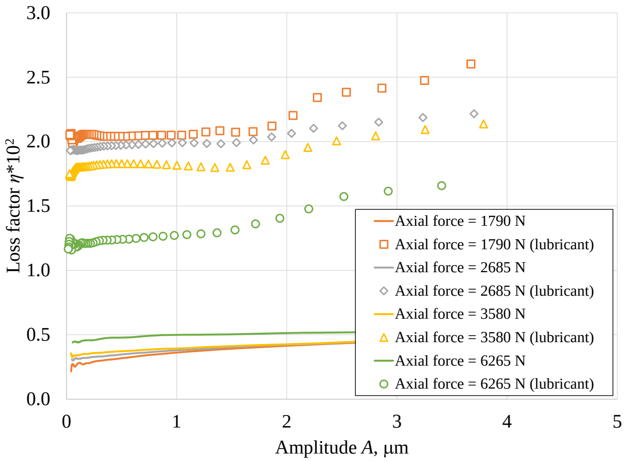

FIGURE 14. COMPARISON OF THE LOSS FACTOR MEASURED ON THE SECOND MODE WITH AND WITHOUT LUBRICANT ON THE DOVETAIL.

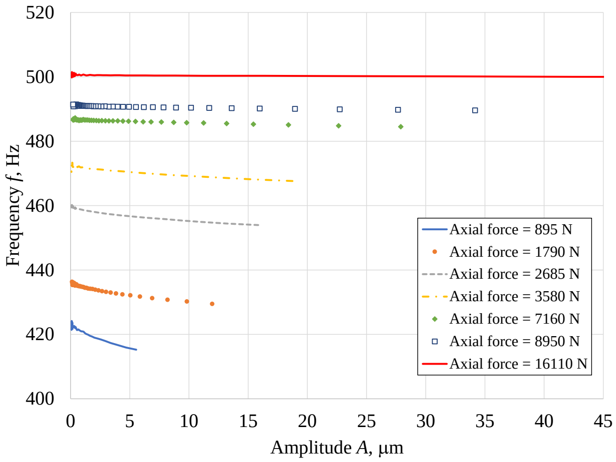

FIGURE 15. NATURAL FREQUENCY MEASURED AS A FUNCTION OF ANTINODE DISPLACEMENT FOR THE FIRST MODE ON THE FIR-TREE.

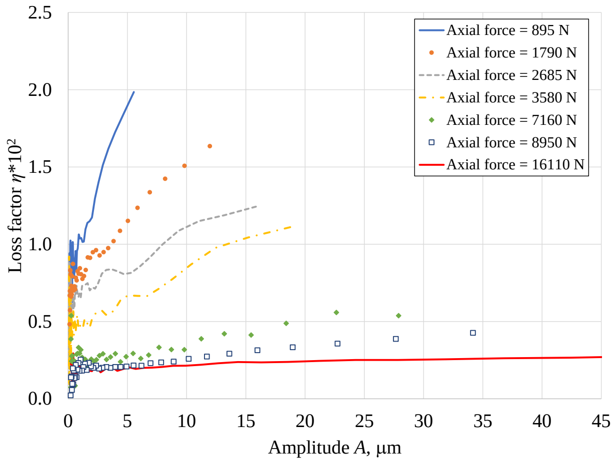

FIGURE 16. LOSS FACTOR MEASURED FOR THE FIRST MODE ON THE FIR-TREE.

effect is negligible.

The second mode of the dovetail was also investigated. Figure 13 shows the natural frequencies as a function of the displacement amplitude of the antinode, which is positioned at about a quarter of the free length of the blade, as indicated by the red dot in Fig. 1. The loss factor is shown in Fig. 14 for both dry and lubricated contacts. With dry contacts, the loss factor is constant and it is weakly affected by axial forces. This behavior is consistent with stick conditions and in fact there is no evidence of slip even at low axial forces. The measured loss factor on lubricated contacts increases with amplitude even if the peak was not reached because the vibration amplitude was too small and full sliding conditions were not achieved.

Tests were also performed on a fir-tree type attachment. Figure 15 depicts the natural frequencies of the first mode for different axial forces. Sliding occurs at low axial forces, as demonstrated by the frequency decreasing with amplitude. The loss factor, see Fig. 16, increases with amplitude without reaching the expected maximum. The natural frequency in stick conditions at varying normal force are shown for the first and second mode in Fig. 17 and Fig. 18 respectively.

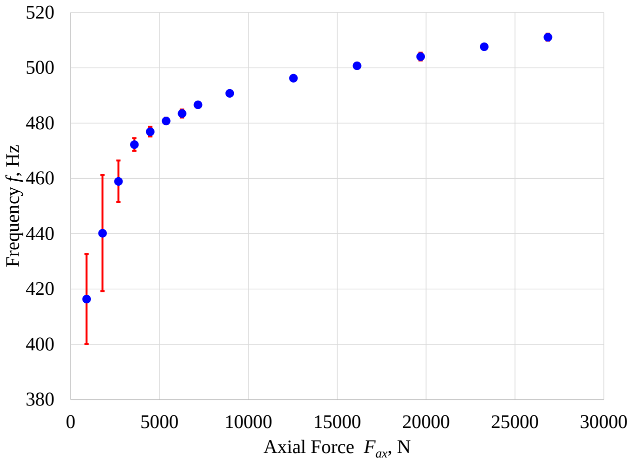

FIGURE 17. NATURAL FREQUENCY FOR LOW DISPLACEMENT AMPLITUDE OF THE FIRST MODE FOR THE FIR-TREE. FREQUENCIES ARE PLOTTED AS A FUNCTION OF THE AXIAL FORCE AND WITH 2.58σ BARS.

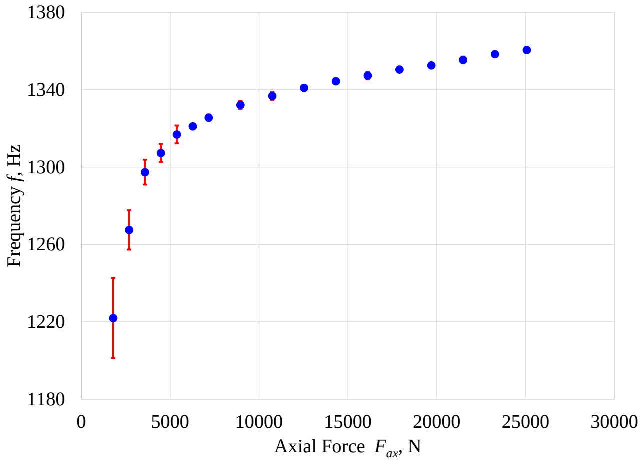

FIGURE 18. NATURAL FREQUENCY FOR LOW DISPLACEMENT AMPLITUDE OF THE SECOND MODE FOR THE FIR-TREE. FREQUENCIES ARE PLOTTED AS A FUNCTION OF THE AXIAL FORCE AND WITH 2.58σ BARS.

CONCLUSIONS

This paper has presented the results of an experimental campaign aimed at studying the damping generated at the root of the blade. For this purpose a test rig capable of loading a dummy blade with different forces was used. An excitation system with virtual non-contact capabilities was utilized to excite the blade and record clean signal for further post-processing. A simplified model with a single dof was used to qualitatively understand what parameters drive the phenomenon. The main findings are listed below.

- The loss factor shows two distinct regions: at low vibration amplitudes the stick regime is predominant while at higher amplitudes the contact is in slip condition. According to the theoretical model the loss factor attains its maximum value in the slip regime and then it decreases with amplitude.
- At low axial forces the damping capabilities of the blade root are remarkable. The maximum loss factor is close to 10 % but values higher than 2% are found also for large amplitudes. At high axial forces the damping capabilities decreases dramatically: for axial force greater than approximately 9 kN the damping of the root is negligible.
- The stick and slip transition is also clearly visible in the natural frequency diagram. At the onset of the slip regime the natural frequencies show a valley that is not predicted by the theoretical model. The natural frequencies in stick condition are related to the contact stiffness.
- The trend of the natural frequencies in stick condition allows us to understand that the ratio between the contact stiffness and the stiffness of the whole system is decreasing with the axial forces. This experimental evidence confirms the behavior emphasized by the simplified model according to which the decreasing of the peak of the loss factor is caused by the decreasing of the ratio between the contact stiffness and the stiffness of the whole system.
- The fir-tree type attachment is stiffer than the dovetail type. The amplitude vibration achieved is smaller, especially at low axial forces, so that the full sliding condition was not triggered. Similar behavior was seen for the second mode, which is stiffer than the first, and also in this case sliding conditions were not achieved.

A second set of data was obtained with lubricated contact surfaces resulting in a lower friction coefficient.

- The comparison between dry and lubricated conditions confirm again the behavior predicted by the simplified model. A lower friction coefficient moves the transition between stick and slip regimes to lower amplitude but it does not affect the peak of the loss factor.

REFERENCES

[1] Cowles, B. A., 1996. “High cycle fatigue in aircraft gas turbines - an industry perspective”. *International Journal of Fracture*, ***80***(2-3), apr, pp. 147–163.

[2] Griffin, J. H., 1980. “Friction damping of resonant stresses in gas turbine engine airfoils”. *J. Eng. Power-Trans. ASME*, ***102***(2), pp. 329–333.

[3] Lavella, M., and Botto, D., 2018. “Fretting fatigue analysis of additively manufactured blade root made of intermetal-

lic ti-48al-2cr-2nb alloy at high temperature". *Materials, **11***(7), jun, p. 1052.

[4] Lavella, M., and Botto, D., 2019. "Fretting wear of alloy steels at the blade tip of steam turbines". *Wear, **426-427***, apr, pp. 735–740.

[5] Menq, C. H., Griffin, J. H., and Bielak, J., 1986. "The influence of microslip on vibratory response, part II: A comparison with experimental results". *J. Sound Vibr., **107***(2), pp. 295–307.

[6] Goodman, L., and Klumpp, J., 1956. "Analysis of slip damping with reference to turbine-blade vibration". *J. Appl. Mech., **23***, pp. 421–429.

[7] Jones, D. I. G., 1979. Vibrations of a compressor blade with slip at root. Tech. rep., Air force Wright Aeronautical Laboratories.

[8] Srinivasan, A. V., Cutts, D. G., and Sridhar, S., 1981. Turbojet engine blade damping. Tech. rep., United Technologies Research Center.

[9] Umer, M., and Botto, D. "Measurement of contact parameters on under-platform dampers coupled with blade dynamics". *Int. J. Mech. Sci., **159***, pp. 450–458.

[10] Umer, M., Gastaldi, C., and Botto, D., 2020. "Friction damping and forced-response of vibrating structures: An insight into model validation". *Int. J. Solids Structures, **202***, Oct., pp. 521–531.

[11] Srinivasan, A. V., 1997. "Flutter and resonant vibration characteristics of engine blades: An IGTI scholar paper". Vol. 4: Manufacturing Materials and Metallurgy; Ceramics; Structures and Dynamics; Controls, Diagnostics and Instrumentation; Education; IGTI Scholar Award of *Turbo Expo: Power for Land, Sea, and Air*, American Society of Mechanical Engineers.

[12] Rao, J. S., Usmani, M. A. W., and Ramakrishnan, C., 1990. "Interface damping in blade attachment region". In Proceedings of 3rd International Conference on Rotordynamics : September 10-12, 1990, Lyon, France, Editions du Centre national de la recherche scientifique.

[13] Rieger, N. F., and McCloskey, T. H., 1990. "Damping properties of steam turbine blades". In Proceedings of 3rd International Conference on Rotordynamics : September 10-12, 1990, Lyon, France, Editions du Centre national de la recherche scientifique.

[14] Allara, M., Filippi, S., and Gola, M. M., 2006. "An experimental method for the measurement of blade-root damping". Vol. 5: Marine; Microturbines and Small Turbomachinery; Oil and Gas Applications; Structures and Dynamics, Parts A and B of *Turbo Expo: Power for Land, Sea, and Air*, pp. 903–912.

[15] Charleux, D., Gibert, C., Thouverez, F., and Dupeux, J., 2006. "Numerical and experimental study of friction damping blade attachments of rotating bladed disks". *Int. J. Rotating Mach., **2006***, pp. 1–13.

[16] Feldman, M., 1994. "Non-linear system vibration analysis using hilbert transform–i. free vibration analysis method 'freevib'". *Mech. Syst. Sig. Process., **8***(2), mar, pp. 119–127.

[17] Firrone, C. M., and Bertino, I., 2015. "Experimental investigation on the damping effectiveness of blade root joints". *Exp. Mech., **55***(5), mar, pp. 981–988.

[18] Nakhla, M., and Vlach, J., 1976. "A piecewise harmonic balance technique for determination of periodic response of nonlinear systems". *IEEE Transactions on Circuits and Systems, **23***(2), feb, pp. 85–91.

[19] Wang, J. H., and Chen, W. K., 1993. "Investigation of the vibration of a blade with friction damper by HBM". *J. Eng. Gas Turbines Power, **115***(2), apr, pp. 294–299.